Materials & Design 210 (2021) 110046

Contents lists available at ScienceDirect

Materials & Design

journal homepage: www.elsevier.com/locate/matdes

Exploration of the influence of different biomimetic designs of 3D printed multi-material artificial spinal disc on the natural mechanics restoration

Zhiyang Yu [a,*], Benjamin Voumard [b], Kristina Shea [a], Tino Stanković [a]

[a] Engineering Design and Computing Laboratory, Dept. of Mechanical and Process Engineering, ETH Zürich, Switzerland
[b] Musculoskeletal Biomechanics, ARTORG Center for Biomedical Engineering Research, University of Bern, Switzerland

HIGHLIGHTS

- Four 3D printed artificial spinal disc designs show nature-mimicking viscoelastic load response.
- The four designs also show comparable instant helical axis and center of rotation to a natural disc.
- Designs that mimic the structure found in a natural disc have big potential for natural mechanics restoration.
- Design with a chainmail-like structure exhibits nature-mimicking nonlinear rotational load response.

GRAPHICAL ABSTRACT

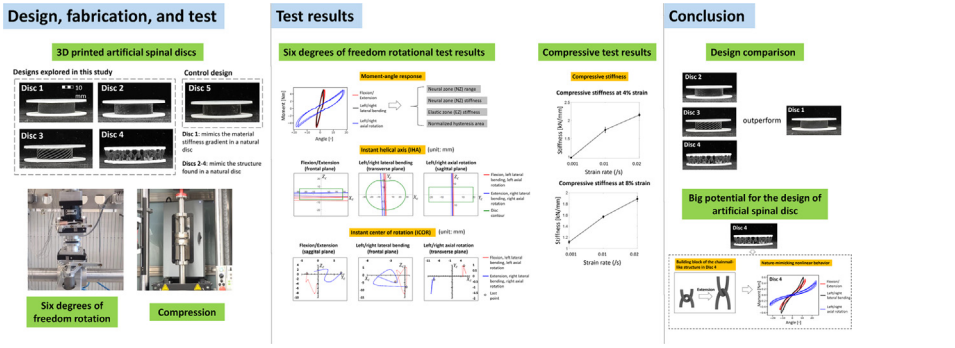

ARTICLE INFO

Article history:
Received 25 May 2021
Revised 18 July 2021
Accepted 15 August 2021
Available online 18 August 2021

Keywords:
Multi-material 3D printing
Artificial spinal disc
In vitro test
Biomimicry
Design evaluation
Architected materials

ABSTRACT

One of the great challenges of artificial spinal disc (ASD) design lies in the reproduction of the complex mechanics of an intervertebral disc (IVD) that is characterized by a viscoelastic, nonlinear, and anisotropic behavior. Although the development of multi-material additive manufacturing (AM) combined with biomimetic design provide new opportunities for the realization of ASDs with complex behavior, the influence of different biomimetic designs on the kinematics of ASD in conjunction with AM is not yet explored. Therefore, this study proposes and fabricates four types of biomimetic, multi-material ASD designs based on mimicking either the material stiffness gradient or the structure found in a natural IVD. The results show that all the designs exhibit a desired viscoelastic behavior, while the ASD design based on a chainmail-like structure exhibits a nature-mimicking nonlinear rotational load response. In terms of restoring the natural trend of an IVD's anisotropic behavior, the ASD design that mimics the structure found in an IVD outperforms the design that solely mimics an IVD's material stiffness gradient. Additionally, all the designs proposed in this study show comparable instant helical axis (IHA) and instant center of rotation (ICOR) to an IVD's regarding their location and moving direction.

1. Introduction

Total disc replacement (TDR) is a widely accepted motion-preserving method to replace a seriously degenerated intervertebral disc (IVD) aimed at restoring the natural motion of the implanted spinal segment [1]. One critical factor that determines

* Corresponding author at: Engineering Design and Computing Laboratory Dept. of Mechanical and Process Engineering, ETH Zürich, Switzerland.
E-mail address: yuz@ethz.ch (Z. Yu).

https://doi.org/10.1016/j.matdes.2021.110046
0264-1275/

TDR's clinical outcomes is the design of the artificial spinal disc (ASD), which is shown to significantly influence the post-implantation kinematics and load transfer within the spinal segment [2,3]. An inappropriate ASD design that fails to reproduce an IVD's natural biomechanics can cause complications such as degeneration of adjacent-level IVDs and facet joint arthrosis due to abnormal load-sharing [4,5].

The majority of existing ASDs are based on an articulating design with an incompressible rigid core that transfers the load completely instead of exhibiting a shock absorption behavior similar to an IVD [6,7]. Besides, the articulating design is incapable of mimicking an IVD's flexural stiffness due to its oversimplified design [8–10]. The resultant abnormal motion pattern can affect the loading sharing among adjacent-level spinal components that is important for the long-term clinical outcomes of TDR [11]. To provide a nature-mimicking elasticity that is a crucial biomechanical property of the spinal segment [12], next-generation ASDs such as the Rhine ASD [13] are realized based on a monolithic compressible elastomeric design and have been clinically shown to outperform the articulating designs in terms of natural motion recovery, patient satisfaction, and long-term implant survival [2,14,15]. Despite their good performances, the single-material elastomeric design is still suboptimal as it fails to replicate an IVD's anisotropic behavior in different loading scenarios [16]. To improve that, some recent ASD designs either employ biomimicry alone [17,18], or in combination with multi-material additive manufacturing (AM) [19], are proposed to restore the nonlinear and anisotropic behavior of an IVD. Whereas the biomimicry capitalizes on using bio-inspired structures and principles to restore the complex behavior of an IVD [20], such as the design of a fabric-based ASD [21], a fiber-reinforced hydrogel-based ASD [22], and a M6 ASD [23], multi-material AM contributes with its ability to fabricate complex designs with a heterogeneous material distribution in a high precision [24]. The benefit of multi-material AM for ASD design is demonstrated by [19] in which a conceptual design of a fiber-reinforced ASD fabricated with multi-material AM is proposed. Additionally, AM helps to fabricate implants with patient-specific sizes to overcome the limitation of size mismatch that is often present with the current standardized ASD designs and can lead to implant subsidence [25]. The potential of combining biomimicry and AM for the design of patient-specific orthopedic implants to restore nature-mimicking anisotropic behavior is also demonstrated by [26] and [27].

Although the combination of multi-material AM and biomimicry provides new opportunities for the realization of ASDs aimed at natural mechanics restoration, the development of multi-material AM fabricated biomimetic ASD is still in the early stage. The possible reason is that the influences of different biomimetic designs together with AM constraints on the performances of ASDs in restoring the natural mechanics are still unexplored. This lack of knowledge to guide the biomimetic ASD design fabricated with multi-material AM also affects the effectiveness of advanced computational approaches that rely on predefined heuristics and appropriate problem formulations to produce optimal designs [19]. Therefore, this study proposes and systematically analyses the performances of four types of biomimetic, multi-material ASD designs based on mimicking either the material stiffness gradient or the structure found in a natural IVD. An additional fifth design that serves as a control design is also included to explore the effect of different types of biomimicry on the ASD's anisotropic performance. All designs are fabricated using a Stratasys Connex3 Objet500 inkjet-based, multi-material 3D printer as a proof-of-concept fabrication technique and tested in vitro to obtain their rotational and compressive responses. It is to be noted that the biocompatibility of the base materials is out of the scope, while the base materials and 3D printing technique for ASD fabrication can be replaced with 3D printable biocompatible materials and corresponding multi-material 3D printing techniques with an appropriate resolution. The performances of the ASD designs are evaluated using metrics that concern the restoration of an IVD's *quantity* and *quality* of motion. The main contribution of this study is to draw implications from the performances of multiple biomimetic ASD designs for the future biomimetic ASD design fabricated with multi-material AM.

2. Methods

2.1. ASD design rationale

The designs of four biomimetic ASD designs together with a fifth control design are illustrated in Fig. 1. All the ASD designs investigated in this study equate in size to a human lumbar L4-L5 IVD as shown in Fig. 2 [25] and share the same sandwiched structure that is composed of a compliant core and two rigid endplates. The rigid endplates are designed to replace the cartilage endplates to interface with adjacent vertebrae, while the compliant core is designed to provide elasticity in various loading scenarios. All the designs have a sagittal plane symmetry to achieve a symmetric load response in left and right loading scenarios. The explored ASDs have a total height of 14 mm: each endplate has a thickness of 2 mm, and the height of the core equals to 10 mm. The detailed dimensions of each ASD design's components are provided in Table 1. The size of the smallest features in the ASD design is restricted by the minimum allowable printable size of the given 3D printer to obtain reliable mechanical properties [28].

The core of Disc 1 consists of a softer, central cylinder and a stiffer, outer ring to mimic an IVD's composition that consists of a soft nucleus pulposus (NP) surrounded by a stiffer annulus fibrosus (AF). Using a combination of two materials with various stiffnesses, this ASD design is featured by a biomimetic functional gradient found in an IVD at the macro level. This design concept is comparable to the design of a 3D printed, functionally-graded lattice structure for bone implants [29]. The volume ratio of the central cylinder to the whole core in Disc 1 is set to 0.42 to imitate the volume ratio of NP in an IVD [30]. In contrast, Disc 2 and Disc 3 include a criss-cross, fiber-like structure to mimic the structure of the fiber network in an AF that is composed of alternating bias-ply laminae [31]. The fiber-like structure is designed to improve the ASD's torsional resistance as well as to provide progressive load resistance [23], which is realized in Disc 2 using a reinforced composite and in Disc 3 using a stand-alone, fiber-like structure surrounding the central cylinder. The filaments in the fiber-like structure are designed to be oriented at an angle of approximate 60° to the z-axis to mimic the orientation of collagen fibers in an IVD [32]. The design of Disc 3 is analogous to the design of a M6 ASD in the market [23].

The design of Disc 4 differs from Disc 3 by having the surrounding structure realized as a chainmail-like structure. The basic building block of the chainmail-like structure, as illustrated in Fig. 3, consists of two half elliptical rings that exhibit an asymmetric load response under tension and compression due to its movable, separable joint. Namely, the building block is featured by zero load resistance when in a compressive state and only exhibits resistance when in an extended state. Besides, when manufactured with a flexible and extendable material, the filaments in the basic building block are able to align gradually in the tensile direction, which results in a gradual increase in its load resistance. These two properties are also features of an IVD's collagen fibers that likewise have negligible compressive resistance and are able to gradually un-crimp upon loading. The number of building blocks in Disc 4 is determined by the size of individual building blocks

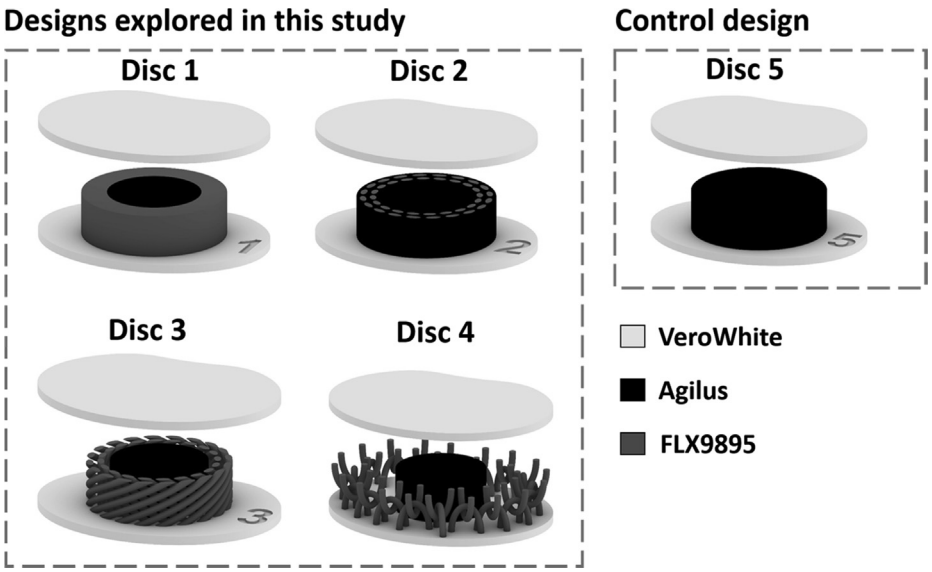

Fig. 1. Four biomimetic, multi-material ASD designs explored in this study together with a control design. The ASD designs share the same overall design that consists of two stiff endplates and a compliant core. The endplates are kept unchanged among the five designs, while the soft core is varied. The core in Disc 1 consists of a softer, central cylinder and a stiffer, outer ring to mimic the functional stiffness gradient in an IVD at the macro level. The core of Disc 2 is analogous to a fiber-reinforced matrix composite, while the core of Disc 3 consists of a soft, central cylinder and a stiffer, criss-cross, fiber-like structure that surrounds the central cylinder. Both Disc 2 and Disc 3 include a criss-cross, fiber-like structure to mimic the fiber network in an IVD. The core of Disc 4 is composed of a soft, central cylinder and a surrounding chainmail-like structure that shares similar features as the fiber network in an IVD. Disc 5 is the control design whose core is made from a single material to explore the effect of different types of biomimicry on the ASD's anisotropic performance. The stiffest building material referred to as VeroWhite ($E \approx 2$ GPa) is used to fabricate the rigid endplates that sandwich the core, while the two flexible, rubber-like materials referred to as Agilus ($E \approx 0.5$ MPa) and FLX9895 ($E \approx 5$ MPa) are used for the fabrication of the compliant core.

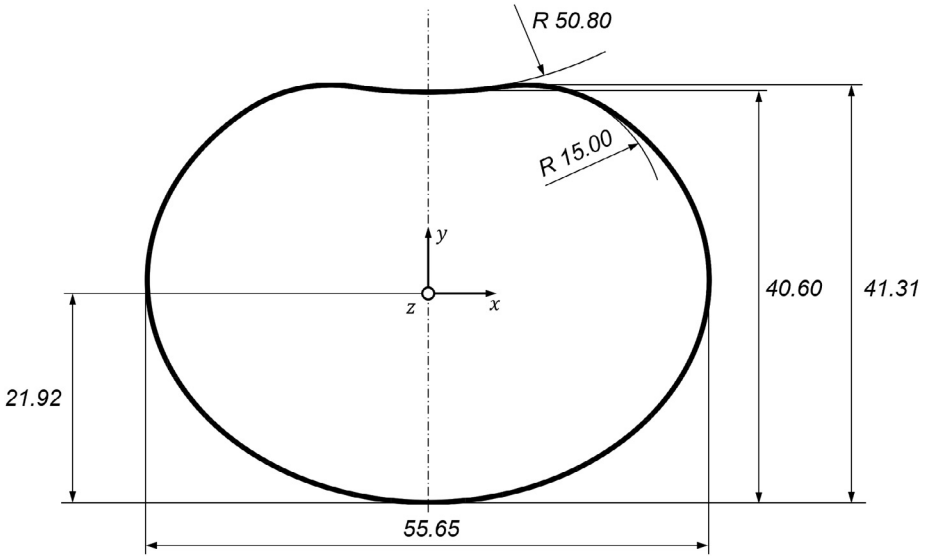

Fig. 2. The dimensions of the ASD designs proposed in this study (unit: mm). The top view of the design space of the ASD design that equals to the size of a human lumbar L4-L5 disc is shown. The height is equal to 14 mm measured in the *z*-direction.

and the ASD design space to avoid overlap. The building blocks in Disc 4 are positioned at the periphery of the endplates to amplify the building blocks' contribution to the ASD's rotational response by maximizing their level arms. This innovative design is intended to achieve behaviors that otherwise cannot be achieved by the given 3D printing materials or other designs presented in this study. Disc 5, which has a single-material cylindrical core with a diameter of 34 mm, works as a control design to explore the effect of different types of biomimicry on the ASD's anisotropic performance.

2.2. Mechanical testing

The test facilities used to measure the rotational and compressive responses of the ASD specimens are shown in Fig. 4. The rotational responses of the specimens are measured using a custom six degrees of freedom (DOFs), computer-controlled spine testing system as shown in Fig. 4 (A) [33] where the motion of the specimens is recorded using an optoelectronic motion analysis system (Optotrak Certus, NorthernDigital, Canada) and the forces and torques are measured using a six-axis load cell (MC3A, AMTI, U.S.A.).

Table 1
List of the dimensions of the components in the cores of Discs 1–4. The filament in the fiber-like structure and the chainmail-like structure is referred to as "fiber" in the table.

Disc 1		Disc 2					
Central cylinder	Outer ring	Matrix	Fiber-like structure				
Diameter	Outer diameter	Diameter	Fiber diameter (Fiber layer thickness)	Diameter of the inner fiber layer (Center line)	Diameter of the outer fiber layer (Center line)	Fiber orientation	Total amount of fibers
22 mm	34 mm	34 mm	1.6 mm	26 mm	31 mm	~60° to the z-axis	40 (20/layer)
Disc 3		**Disc 4**					
Central cylinder	Stand-alone fiber-like structure	Central cylinder	Chainmail-like structure				
22 mm	The design parameters are the same as those of the fiber-like structure in Disc 2	22 mm	Fiber diameter	Diameter of the elliptical rings in a chainmail building block		Amount of chainmail building blocks	
			1.6 mm	Major axis	Minor axis	19	
				13 mm	7.2 mm		

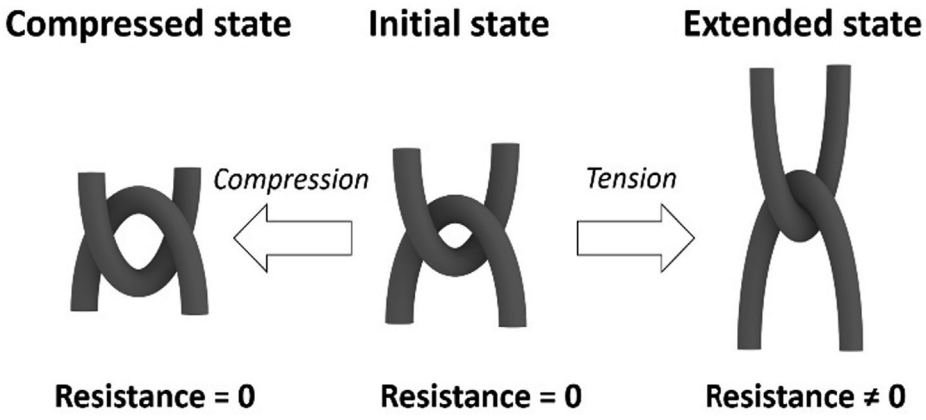

Fig. 3. Design and mechanism of the basic building block of the chainmail-like structure in Disc 4. Due to the movable, separable joint, the building black shows negligible resistance in compression and only shows resistance under tensile loads. In addition, when manufactured with a flexible and extendable material, the filaments in the basic building block are able to align gradually in the tensile direction, which leads to a gradual increase in its load resistance.

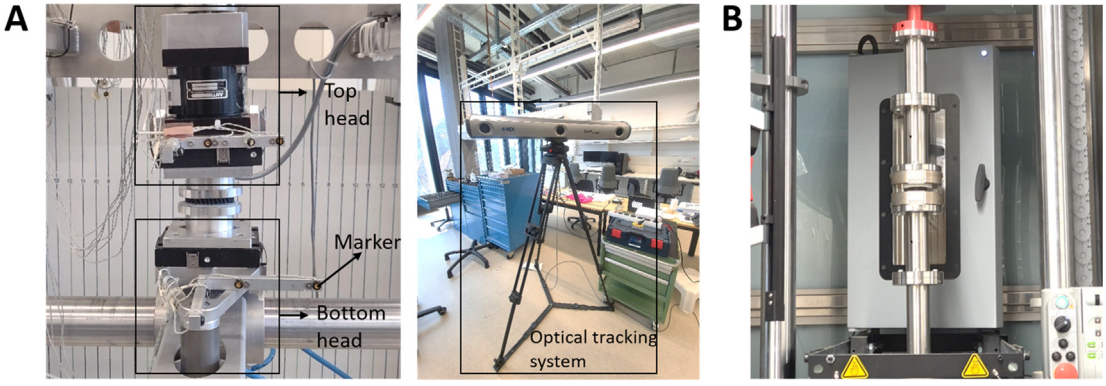

Fig. 4. Test facilities for performing rotational and compression testing of the ASD specimens. (A) The rotational test facility [33] includes a six-axis load cell (left) with a top and bottom head where the markers are attached, and an optical tracking system (right) that records the markers' locations in the three-dimensional space. (B) The compressive test facility: the Instron ElectroPuls E3000 testing machine with a Dynacell loadcell of 3 kN capacity.

Additionally, an Instron ElectroPuls E3000 testing machine with a Dynacell loadcell of 3 kN capacity as shown in Fig. 4 (B) is used to measure the compressive response of the ASD specimens. The metrics used to evaluate the performances of the ASD designs involve the analyses of the specimen's rotational response with respect to the initial neutral zone (NZ) with a minimum stiffness, the subsequent elastic zone (EZ) with a comparatively high stiffness, and the hysteresis area. Additionally, the specimen's compressive stiffness is derived from its compressive response. The metrics selection is based on the recommended in vitro testing criteria for ASD evaluation [34], while the detailed definitions of the metrics are provided in Appendix A. The analysis of the rotational response also includes instant helical axis (IHA) and instant center of rotation (ICOR) that provide temporal three-dimensional

and two-dimensional information for describing an ASD's motion pathway to more precisely evaluate the ASD's performances [35,36]. ICOR pattern has been used in many studies to identify abnormal motions, as it is closely related to spinal segment stability and load sharing among other spinal tissues [37–40]. The following sections present the detailed mechanical testing procedures, while the procedure of the test data analysis for deriving the metrics from the specimen's rotational and compressive load responses is given in Appendix B.

Rotational test: The rotational load responses of the specimens in six DOFs are measured in this step. The specimen is rigidly connected to the test facility using two aluminum plates (one at the top and one at the bottom) that are connected to the endplates of the specimen using a superglue (cyanoacrylate adhesive, UHU, Germany) to avoid the relative movement between the aluminum plates and the specimen. The plates are designed to have a matching geometry with the specimen's endplates to improve fixation stability. Aluminum is used to manufacture the plates to minimize the effect of the plates' stiffness on the test results. The testing system applies pure moments that are recorded by the six-DOF load cell, while the resultant motions of the top and bottom endplates of the specimen are obtained based on the markers attached to the top and bottom rigid test facilities.

The specimen is loaded under a displacement control mode with a loading rate of 1°/s (ramp-loading). Each specimen is loaded sequentially in six DOFs illustrated in Fig. 5 (A) based on the disc coordinate system shown in Fig. 5 (B): extension (negative rotation angle along the *x*-axis), flexion (positive rotation angle along the *x*-axis), left and right lateral bending (LB) (positive and negative rotation angle along the *y*-axis, respectively), right and left axial rotation (AR) (negative and positive rotation angle along the z-axis, respectively). In each loading scenario, a pure moment is added at a certain DOF and repeated for three cycles, while the specimen is allowed to move freely in the remaining five unloaded DOFs, thus allowing for a coupled motion. The stopping criteria for all the specimens are when the maximum loading angle is reached or the maximum allowable moment of the testing system, i.e., 5 Nm, is reached. The maximum loading angle is set to 14° for flexion/extension, 12° for left/right LB, and 24° for left/right AR, which are determined to avoid material failure of the specimens. The loading process is paused for two seconds when the loading process is stopped in each DOF.

Compression test: Each specimen is loaded until a 10% strain with a strain rate of 0.001, 0.01, 0.02 s^{-1} sequentially to examine the effect of strain rate on the compressive load response of the specimen. A ten-minute relaxing time is used for all the specimens between subsequent tests to allow for stress relaxation.

3. Results

3.1. 3D printed ASD specimens

Five specimens of each ASD design are fabricated for the subsequent mechanical testing, while the amount of specimens required is determined according to the ASTM norm for in vitro ASD tests (F2346-18). With the detailed material constituents of each ASD design illustrated in Fig. 1, examples of the 3D printed specimens

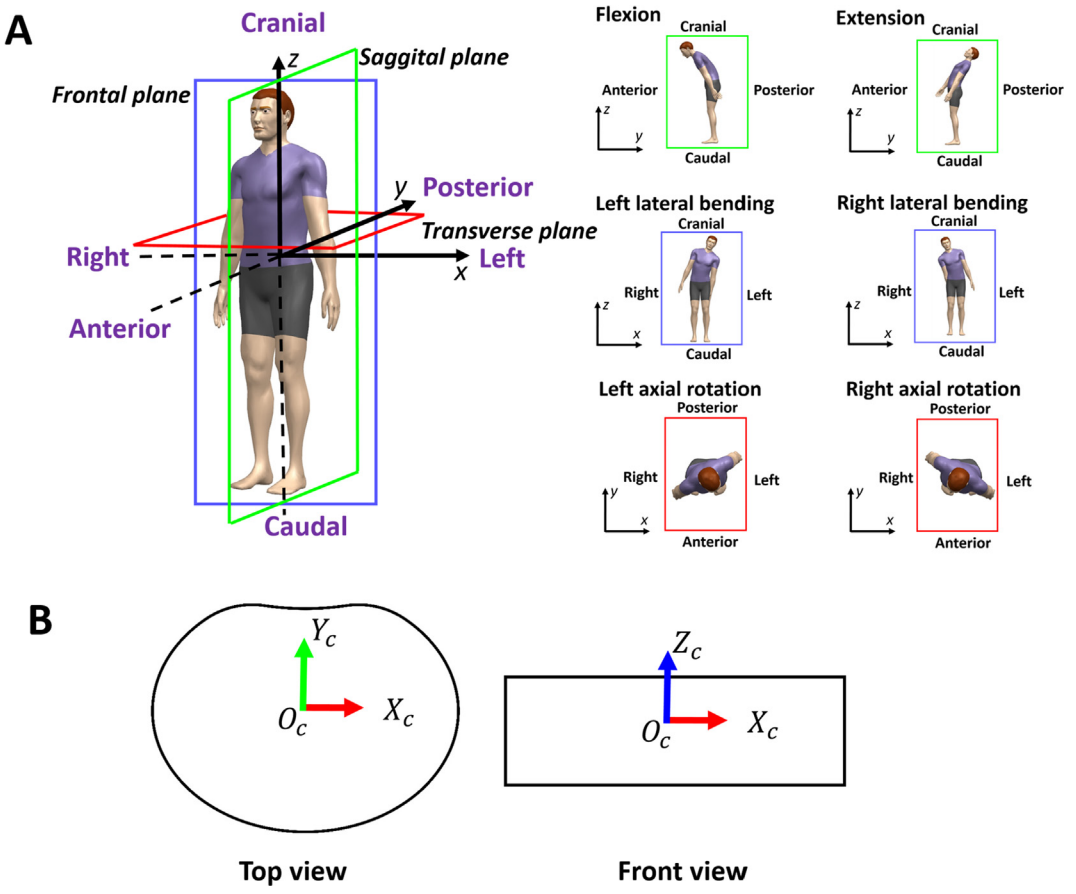

Fig. 5. Illustration of six rotational loading scenarios and definition of the disc coordinate system. (A) Six rotational loading scenarios defined based on anatomical planes and directions: flexion/extension, left/right lateral bending (LB), and left/right axial rotation (AR). (B) The disc coordinate system denoted by $O_cX_cY_cZ_c$ whose origin is in the geometric center of the ASD design.

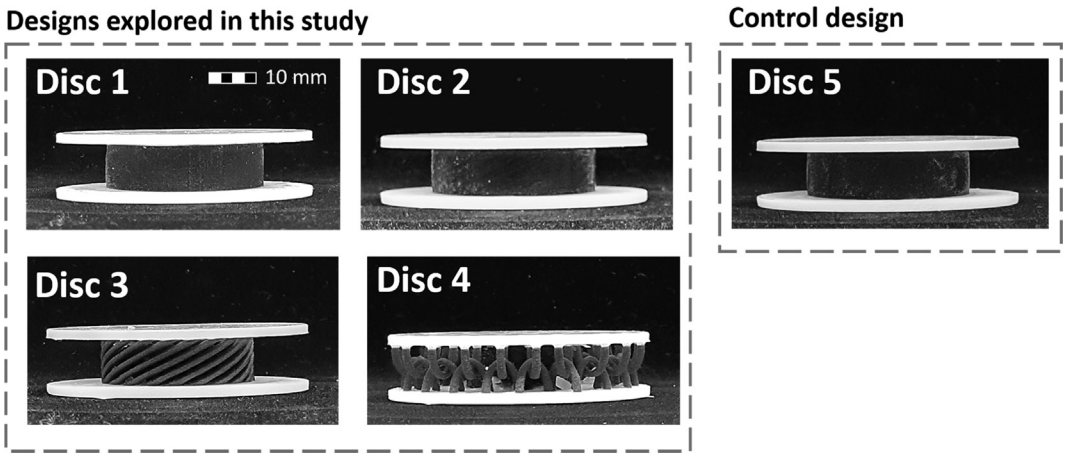

Fig. 6. Examples of 3D printed specimens of the five ASD designs. The specimens are manufactured with the "matte" print option provided by the Stratasys Connex3 Objet500 inkjet-based, multi-material 3D printer and printed in a layer-by-layer manner along the Z_c axis of the disc coordinate system, while the print head moves along the X_c axis of the disc coordinate system while printing each layer.

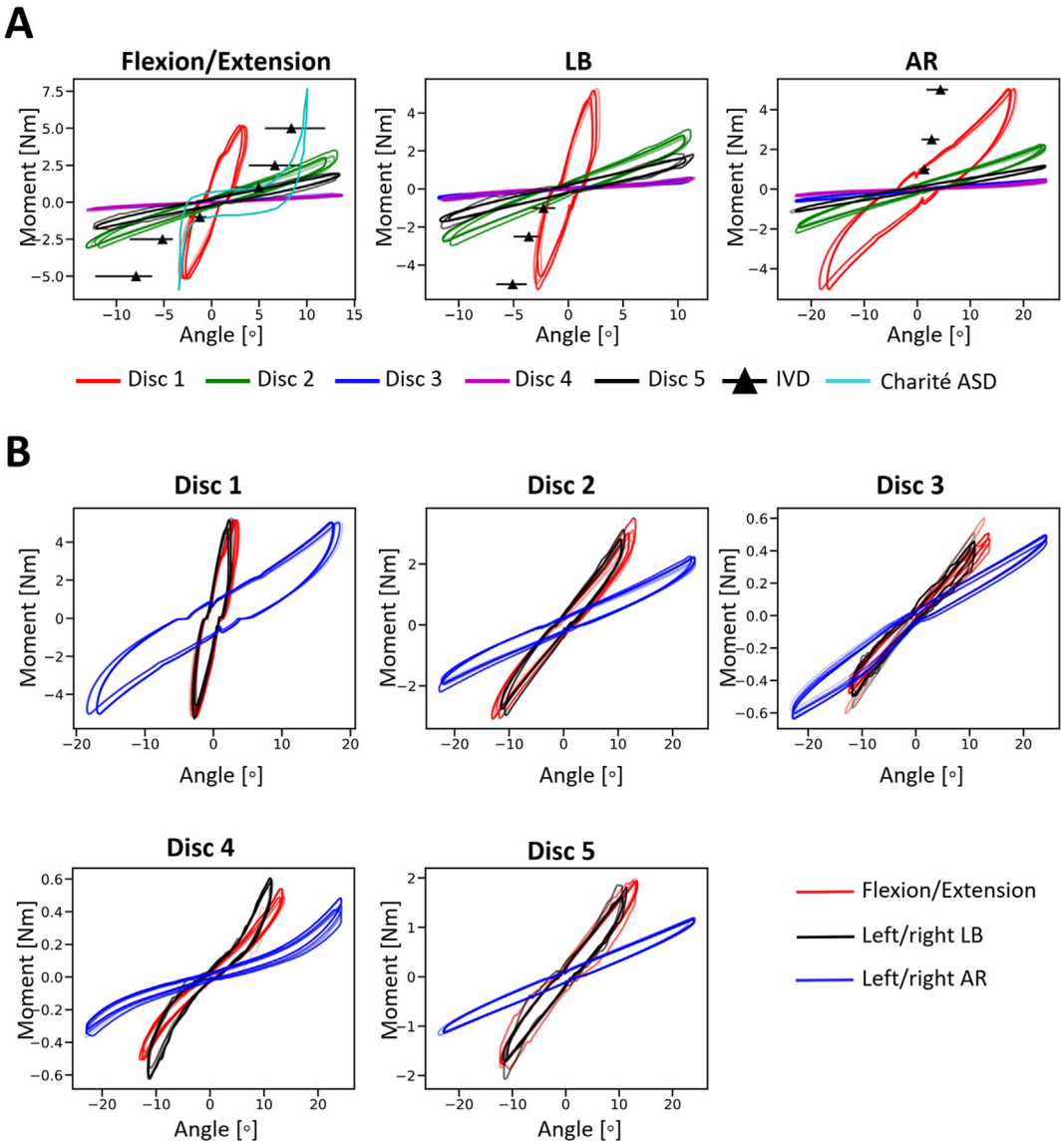

Fig. 7. The rotational responses of all the specimens of the five ASD designs. The responses of different specimens that belong to the same ASD design are differentiated using different color transparencies. (A) Comparison of the rotational responses of the five ASD designs with a human lumbar L4-L5 IVD's [43] and a Charité ASD's [11]. The IVD rotational response is demonstrated using the median, minimum and maximum angle at a given moment. Due to data availability the comparison is not provided for all the loading scenarios. (B) The detailed rotational responses of all the specimens of the five ASD designs.

of the five ASD designs are shown in Fig. 6. The specimens are manufactured with the "matte" print option provided by the Stratasys Connex3 Objet500 inkjet-based, multi-material 3D printer in a layer-by-layer manner along the Z_c axis of the disc coordinate system, while the print head moves along the X_c axis of the disc coordinate system while printing each layer. The support material of the specimens is then removed right after printing using a water jet and the specimens are stored in a dark place for ~ 24 h before mechanical testing to minimize the influence of material aging on the specimens' mechanical properties [41].

3.2. Rotational and compressive load responses

The data analysis of the rotational and compressive responses of the specimens as stated in Appendix B is performed using an in-house developed script. The raw data of the rotational and compressive responses of all the specimens together with the video that illustrates the mechanical testing procedure are provided in [42] and Supplementary Video, respectively. Fig. 7 shows the rotational responses of the five ASD designs in six rotational loading scenarios, while the metrics derived from the rotational responses

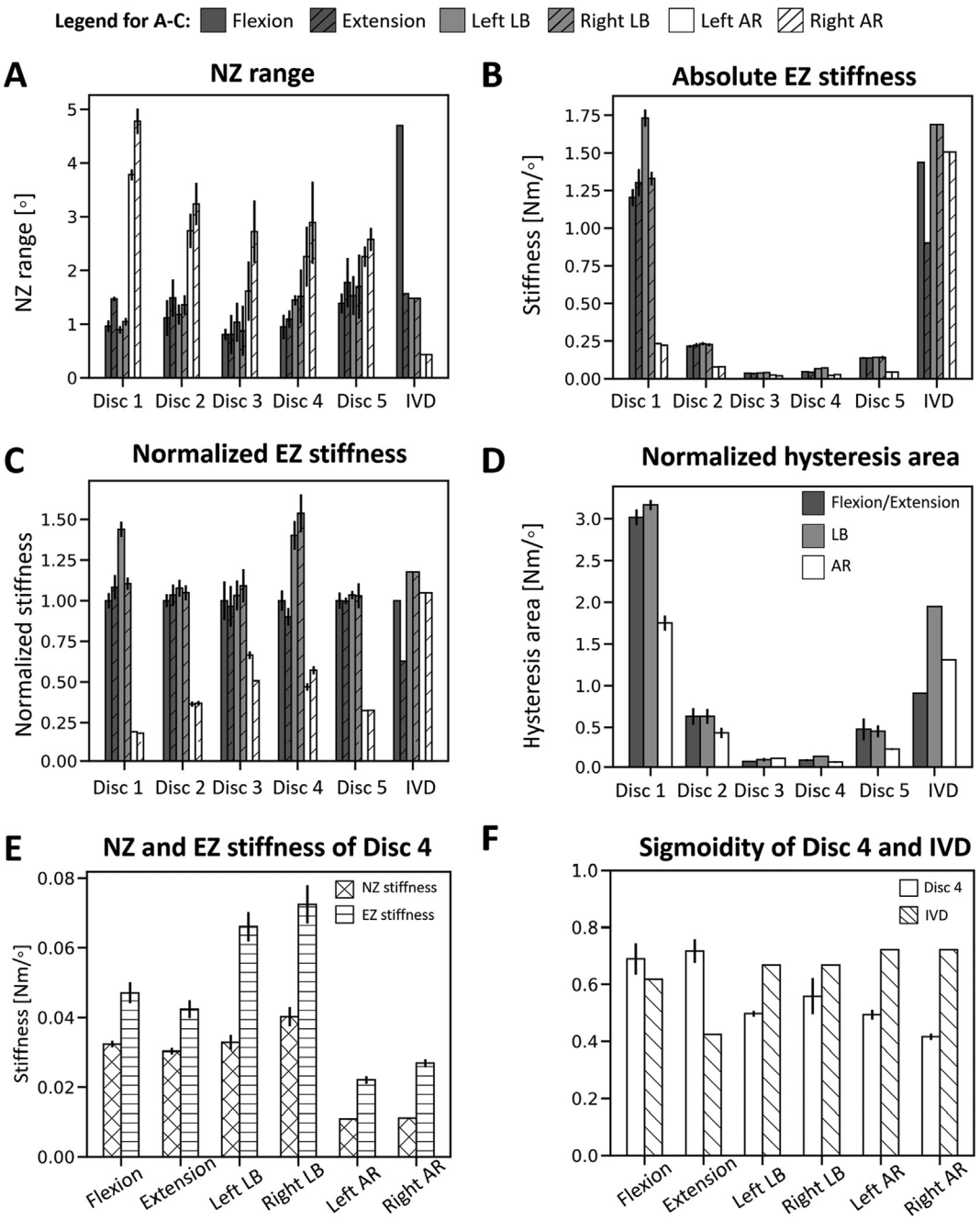

Fig. 8. Summary of the metrics that describe the performances of the five ASD designs in six rotational loading scenarios. (A) NZ range. (B) Absolute EZ stiffness. (C) Normalized EZ stiffness (the EZ stiffness of each specimen is normalized to its corresponding EZ stiffness in flexion). (D) Normalized hysteresis area. The NZ range, EZ stiffness, and sigmoidity of the IVD are referenced from [43], while the normalized hysteresis area of IVD is referenced from [44].

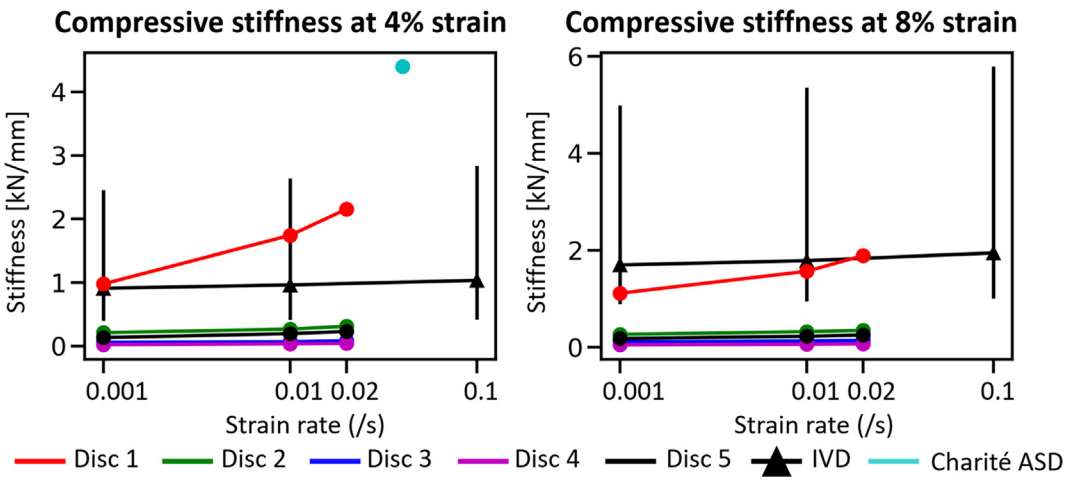

Fig. 9. The compressive stiffnesses of the five ASD designs at 4% and 8% strain. The compressive stiffnesses of the five ASD designs are compared to a human lumbar IVD's [45] and a Charité ASD's [46]. The vertical error bars of the IVD stiffness show the minimum and maximum stiffness of an IVD under a certain strain rate based on the findings from the literature [45], while the standard deviations of the compressive stiffnesses of the five ASD designs are all less than 0.05 kN/mm and are thus not shown in the figure.

for evaluating the ASD's performances are summarized and compared to an IVD's in Fig. 8 [43,44]. The compressive stiffnesses of the five ASD designs at 4% and 8% strain under different strain rates are presented and compared to an IVD's [45] and a Charité ASD's [46] in Fig. 9.

(Supplementary video)

3.3. Instant helical axis (IHA) and instant center of rotation (ICOR)

Based on the disc coordinate system shown in Fig. 5 (B), five IHAs and ICORs are calculated in equally incremental time steps that span from the specimen's neutral position to the maximally loaded position in each rotational loading scenario. For illustration clarity, Fig. 10 presents the 3D isometric views and the most representative 2D projected views of the IHAs of one specimen of each ASD design in six rotational loading scenarios, while the additional 2D projected views of the IHA are provided in Fig. 1 of Supplementary Material. Besides, Fig. 10 provides a comparison of the IHAs of the ASD designs with those of a Charité ASD and an IVD [3,47]. Fig. 11 shows the corresponding ICORs of one specimen of each ASD design in six rotational loading scenarios by intersecting the IHAs in flexion/extension, LB, and AR with the sagittal plane, the frontal plane, and the transverse plane, respectively. The comparison of the ICORs of the ASD designs with those of an IVD and a Charité ASD [48] is also presented in Fig. 11. The ICORs of all the five specimens of each ASD design are provided in Figs. 2-7 of Supplementary Material.

4. Discussion

The Stratasys Connex3 Objet500 inkjet-based, multi-material 3D printer, which is based on the PolyJet printing technique, is selected for the ASD fabrication due to its high resolution and high dimension accuracy [49,50]. Generally, the dimensional standard deviation increases with the decrease of the feature size with the PolyJet 3D printing technique [51]. Based on the disc coordinate system defined in Fig. 5 (B) and the printing orientation stated in Section 4.1, the relative dimensional standard deviations of the smallest feature of the proposed ASDs fabricated with support materials (i.e., 1.6 mm as shown in Table 1) are ~2.29%, ~0.96%, and ~1.83% in the X_c, Y_c, and Z_c direction, respectively [51]. The negligible effect of the dimensional deviation on the mechanical responses of the fabricated ASDs is verified by the good agreement for the load responses among the five specimens that belong to the same ASD design (Fig. 7). The good agreement for load resposes also proves the performance repeatability of the 3D fabricated specimens with the given 3D printer. Besides, it is to be noted that layer deposition direction, i.e., the object printing orientation, can influence the mechanical properties of the 3D fabricated parts [41]. It is shown that parts fabricated using VeroWhite with a longitudinal alignment along the direction vertical to the printing bed have a ~8% lower Young's modulus, a ~40% lower ultimate strength, and a ~72% lower total strain at break compared to parts with a longitudinal alignment along the direction parallel to the printing bed [41]. The variance in mechanical properties among parts fabricated with different orientations is mostly attributed to the layer-by-layer printing process. Additional factors that can contribute to the variance are differences in UV exposure and the number of active nozzles [41]. However, there lacks extensive data from the literature to characterize and model the influence of build orientation on the mechanical properties of parts with respect to all possible build orientations and all the materials provided by the given 3D printer. Therefore, future studies are suggested to follow the same printing orientation used in this study for results reproducibility.

The rotational load responses of all the ASD designs are featured by a hysteresis loop with energy dissipation typical for viscoelastic materials. All the ASD designs except Disc 4 show a mostly linear rotational response. The nature-mimicking nonlinear rotational response of Disc 4 is attributed to the unique shape change ability of its chainmail-like structure, which is featured by lower resistance under small loads when the filaments are loose and high resistance under big loads when the filaments are strained. All the ASD designs show a smooth rotational response, as well as lower AR stiffnesses compared to their corresponding stiffnesses in flexion/extension and LB (Fig. 7). In contrast, Charité ASD is characterized by negligible load resistance at small rotational angles, and a sudden increase in its load resistance when the rotation angle reaches a certain value. The two behavior patterns typical for an IVD and a ball-and-socket ASD, such as a Charité ASD, are defined as soft and hard load constraints, respectively (Fig. 12). All the five ASD designs explored in this study differ from a Charité ASD by showing a nature-mimicking soft constraint. Regarding the compressive responses, all the ASD designs are compressible and show compressive stiffnesses closer to an IVD's compared to a Charité ASD's, as the Charité ASD is nearly incompressible with

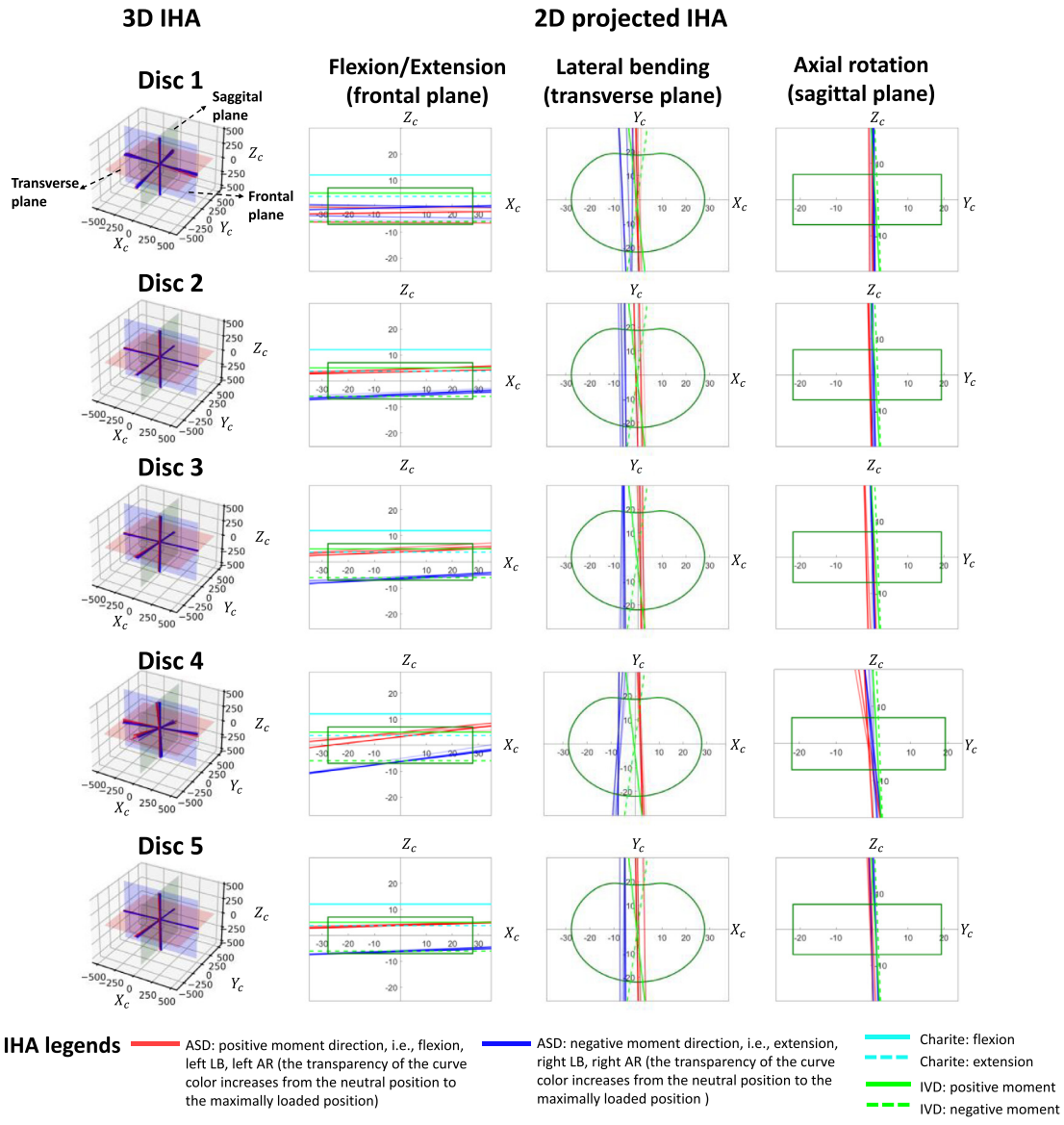

Fig. 10. IHAs of the five ASD designs in six rotational loading scenarios (unit: mm). The IHAs of the five specimens belonging to the same ASD design are comparable in terms of location and moving direction, therefore for illustration clarity only IHAs of one specimen of each ASD design are shown. In each loading scenario, five IHAs are calculated in equally incremental time steps that span from the neutral position to the maximally loaded position. The first column of the figure shows the 3D isometric views of the IHAs, while the other columns show the representative 2D projected views of the IHAs in flexion/extension, LB, and AR on three orthogonal, two-dimensional planes, i.e., X_CZ_C, X_CY_C, Y_CZ_C, respectively. The contour of the ASD is illustrated using green solid line, while the IHAs of the Charité ASD and the IVD are referenced from [347]. (For interpretation of the references to color in this figure legend, the reader is referred to the web version of this article.)

an unnaturally high compressive stiffness, as shown in Fig. 9. Among all the ASD designs, the rotational and compressive responses of Disc 1 mostly closely mimic those of an IVD in terms of absolute values. It is to be noted that there is a high individual-level variation of an IVD's mechanics [3,52], therefore the biomechanical responses of the IVD used for comparison in this study can only be interpreted as one possibility for performing relative comparisons.

The NZ ranges of the five ASD designs (Fig. 8 (A)) are statistically significantly different in left/right AR ($p < .001$). Generally, the NZ ranges of the five ASD designs are close to an IVD's in extension and LB, while being higher than an IVD's in AR and lower than an IVD's in flexion [53]. Nevertheless, the NZ ranges of the five ASD designs are closer to an IVD's compared to the much lower NZ ranges after spinal fusion [54] and the much higher NZ ranges based on a Charité ASD [11]. An abnormal laxity/flexibility around the neutral position can lead to an unnatural load distribution within the other spinal components and may lead to pain [55]. EZ stiffness comparison shown in Fig. 8 (B) and Fig. 8 (C) provides insights into the effect of biomimicry type on the ASD's anisotropic performance, while the normalized EZ stiffness (Fig. 8 (C)) facilitates the comparison by having the EZ stiffness of different designs at the same scale. Although Disc 1 shows a comparable bending and compressive stiffness to an IVD's, it lacks the ability of restoring an IVD's torsional stiffness, i.e., AR stiffness. This is shown in Fig. 8 (C) where Disc 1 shows a ~42% reduction in its relative AR stiffness compared to the control design Disc 5, implying that the stiffer outer layer in Disc 1 disproportionally contributes to increasing the bending and torsional stiffnesses. In contrast, compared to the control design Disc 5, the introduction of a fiber-like structure (Disc 2 and Disc 3) and a chainmail-like structure (Disc 4) improves the ASD's relative AR stiffness by ~13%, ~80 %, and ~60 %, respectively. This shows that designs based on mimicking an IVD's structure (Discs 2–4) have greater potential than designs

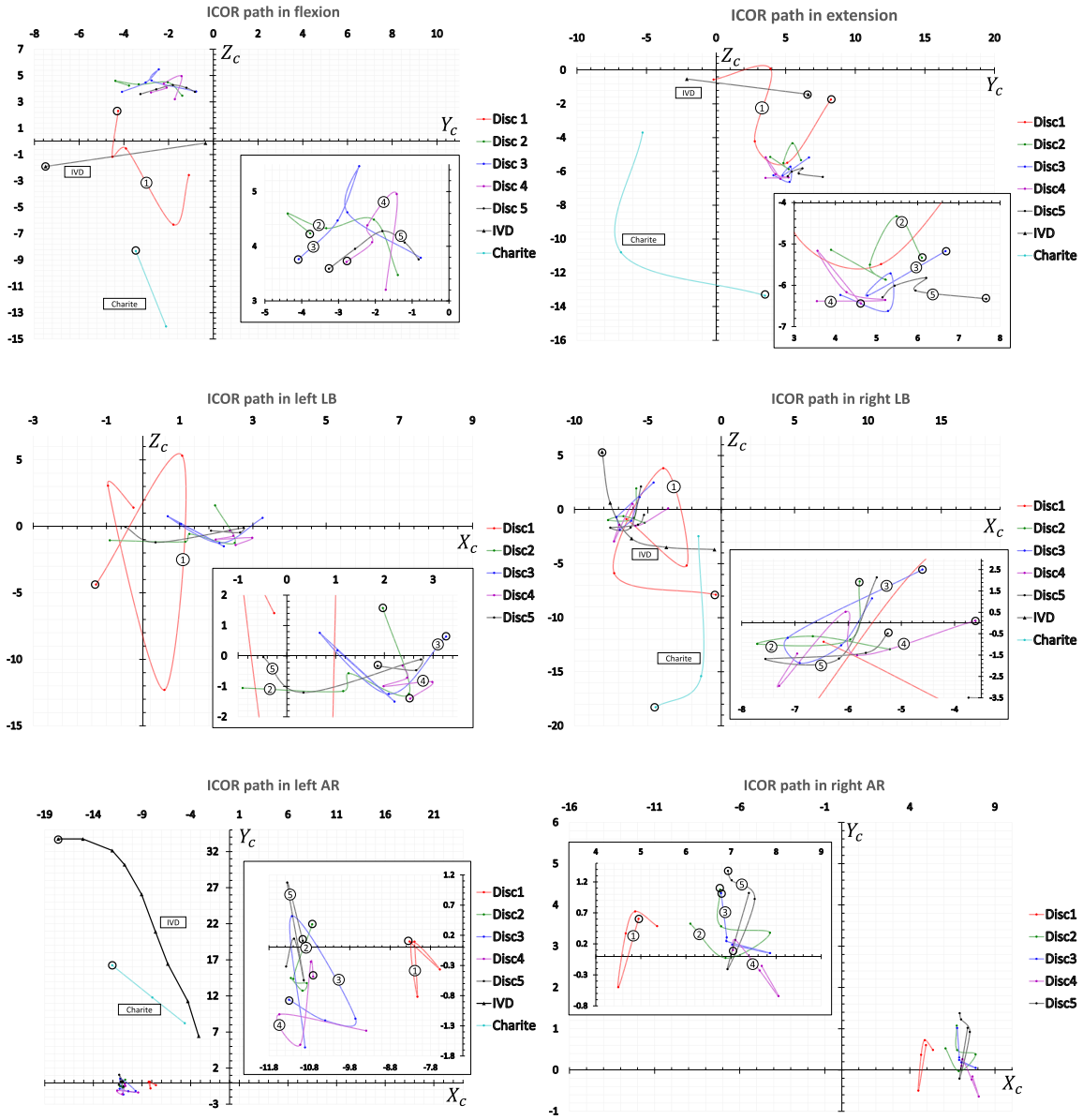

Fig. 11. ICOR and its moving path of the five ASD designs in six rotational loading scenarios (unit: mm). The ICOR is calculated by intersecting the corresponding IHA in flexion/extension, LB, and AR with the sagittal plane, the frontal plane, and the transverse plane, respectively. In each loading scenario, five ICORs are calculated in equally incremental time steps that span from the neutral position to the maximally loaded position. For illustration clarity, only ICORs of one specimen of each design is shown. The black circle marks the end point of the ICOR's moving path illustrated with a smoothed line that interpolates the ICORs in time sequence. To increase readability, insets showing details of the ICOR paths are added to each chart. Due to lack of data from literature, ICOR paths of the five designs are not compared to an IVD's and a Charité ASD's in all the loading scenarios. The ICORs of the IVD and the Charité ASD are referenced from [48].

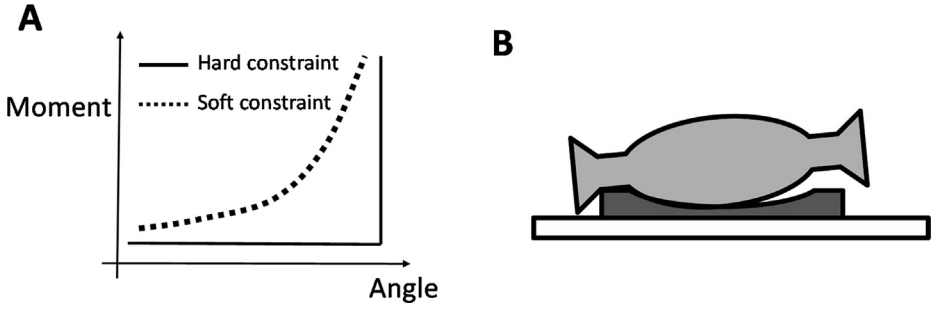

Fig. 12. Illustration of the soft and hard load constraints. (A) The soft load constraint (highlighted with a dotted line), which is featured by a gradual, smooth change in load resistance, is a typical motion pattern of an IVD. In contrast, the hard constraint (highlighted with a solid line) that is featured by a sudden load resistance change is a typical motion pattern of ball-and-socket ASD designs such as a Charité ASD. (B) Cause of the hard load constraint exhibited by the ball-and-socket ASD designs. The ASD's core moves freely relatively to the endplates at small angles and impinges on the endplates after reaching a certain rotation angle, which results in a motion with a hard constraint.

based on only mimicking an IVD's material stiffness gradient (Disc 1) for restoring an IVD's anisotropic behavior.

The normalized hysteresis areas of the five ASD designs (Fig. 8 (D)) show statistically significant differences ($p < .001$) in all the rotational loading scenarios and are positively correlated with the EZ stiffness, which matches the findings from the literature [56]. Disc 4 shows a pronounced nonlinear trend in its rotational load response with distinct NZ and EZ zones (Fig. 8 (E)). Besides, the sigmoidity of Disc 4 in six loading scenarios is comparable to that of an IVD (Fig. 8 (F)). The superior performances of Disc 4 match the finding from literature that demonstrates the great potential of introducing architected materials in the orthopedic implant design [57].

Fig. 10 shows that the IHAs of the five ASD designs are mostly located near the origin of the disc coordinate system in all the loading scenarios and are mainly parallel to the X_c, Y_c, and Z_c axis in flexion/extension, LB, and AR, respectively. In addition, the IHAs of the five ASD designs are more comparable to an IVD's compared to a Charité ASD's regarding the IHA's location and orientation (Fig. 10). The five ASD designs (Fig. 11) also show more comparable ICORs to an IVD's compared to a Charité ASD's regarding the ICOR's location and moving direction in flexion/extension and left/right LB. Specifically, the ICORs of the five ASD designs and the IVD are mostly located near the origin of the disc coordinate system and move more anteriorly, posteriorly, and cranially in flexion, extension, and LB, respectively. In contrast, the ICORs of a Charité ASD show a bigger location variance and unphysiological moving directions such as in right LB. The location deviation of the ICORs of the five ASD designs from an IVD's in left/right AR can be attributed to the lack of facet joint in the mechanical testing performed in this study, as the facet joint is shown to play a significant role in left/right AR [48,58]. The ICOR paths of the IVD and the Charité ASD are interpolated based on three ICORs with a ~3 Nm load interval [48], while the average magnitude of the load interval between ICORs of the five ASD designs is ~0.4 Nm. A smaller interval if between ICORs will amplify the influence of noise. In addition, the ICOR paths of the IVD and Charité ASD are derived from simulation data. Those two factors explain the smoothness of the ICOR paths of the IVD and Charité ASD.

The research performed in this study has some limitations. First, the methodology is based on the assumption of a perfect fixation at the bone-implant interface between the vertebrae and the ASD, while in practice the fixation strength is dependent on the bone-ingrowth level [59]. In addition to ASD design, the difference in fixation strength can also lead to kinematics variations of the implanted spinal segment. Second, this study does not consider the effect of other spinal components, such as the facet joint that is shown to have a significant influence on the spinal segment's biomechanical behavior [60]. Lastly, this study only focuses on the static load responses of the five ASD designs, while their dynamic responses are not measured in this study.

To conclude, this study systematically investigates and compares the performances of four 3D printed, multi-material biomimetic ASD designs to explore the influence of using multi-material AM and biomimicry on the performances of ASD designs. The ASD's performances are evaluated in terms of restoring the unique viscoelastic, nonlinear, and anisotropic behavior of an IVD [61]. Multi-material AM is shown to be a good candidate technology to fabricate various biomimetic ASD designs with a controlled material distribution. All of the four ASD designs show a viscoelastic behavior with nature-mimicking mobile IHA and ICOR, while Disc 4 with a chainmail-like structure exhibits a distinct nature-mimicking nonlinear rotational response. Besides, results show that biomimicry based on mimicking an IVD's structure (Discs 2–4) has greater potential compared to mimicking an IVD's stiffness gradient alone (Disc 1) to restore the natural anisotropic behavior. In summary, this study shows the great potential of multi-material AM and biomimicry for the ASD design and serves as basis for the future development of monolithic, elastomeric ASD for natural mechanics restoration. Based on the material anisotropy in an IVD's AF [62], future studies can involve a material optimization of the favorable biomimetic ASD designs (Discs 2–4) to further improve the ASD's nature-mimicking performances.

CRediT authorship contribution statement

Zhiyang Yu: Conceptualization, Methodology, Software, Formal analysis, Investigation, Resources, Data curation, Writing – original draft, Writing – review & editing, Visualization, Project administration. **Benjamin Voumard:** Resources, Writing – review & editing. **Kristina Shea:** Resources, Writing – review & editing, Supervision. **Tino Stanković:** Conceptualization, Writing – review & editing, Supervision.

Declaration of Competing Interest

The authors declare that they have no known competing financial interests or personal relationships that could have appeared to influence the work reported in this paper.

Acknowledgements

We would like to thank Prof. Dr. Philippe Zysset from ARTORG Center for Biomedical Engineering Research in University of Bern for gracefully allowing us to have the access to their spinal disc test facilities.

Appendix A. Metrics for the performance evaluation of an ASD

This section presents the definition of the metrics that concern both the restoration of an IVD's *quantity* and *quality* of motion. The metrics that belong to the *quantity* of motion are NZ range, NZ stiffness, EZ stiffness, hysteresis area, as well as the compressive stiffness under different strain rates. The evaluated metrics that belong to the *quality* of motion are sigmoidity, IHA, and ICOR. As shown in Fig. 13, the nonlinear load response of an IVD is characterized by an initial NZ at small displacements, followed by an EZ at bigger displacements [63]. The NZ range is defined as the angle difference between two zero moment points in two loading phases [43]. For each loading phase or scenario, the NZ range is defined as the angle difference between the neutral position and the zero moment point. The NZ range is used to quantify the range over which the IVD moves freely with little load resistance and is a measurement of the ASD's laxity. The slopes of the moment–angle load response in NZ (denoted as red dashed line in Fig. 13) and EZ (denoted as green dashed line in Fig. 13) are defined as NZ stiffness and EZ stiffness, respectively. Similarly, the compressive stiffness is defined as the slope of the force–displacement response of the ASD. The NZ and EZ stiffness, together the compressive stiffness, influence the range of motion (ROM) that is defined as the maximum displacement or rotational angle from the initial neutral position to the maximally loaded position. The hysteresis area, which is defined as the area enclosed by the moment–angle curve, describes the energy absorption behavior of an IVD and is related to spine stability in dynamic situations [56]. The normalized hysteresis area is calculated by dividing the hysteresis area by the ROM. Sigmoidity, which evaluates the nonlinearity of the ASD's rotational response, is defined as the ratio of NZ stiffness and EZ stiffness.

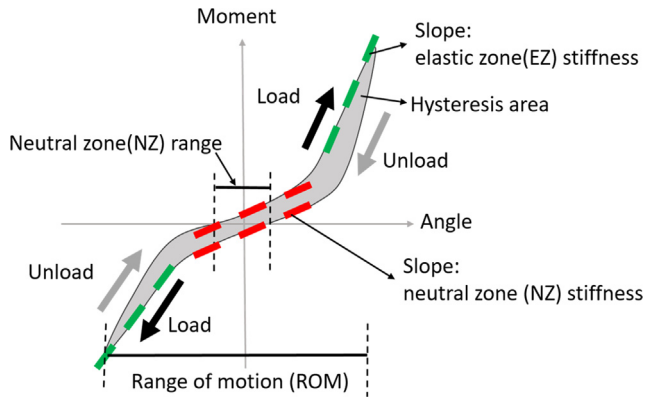

Fig. 13. Typical rotational response of an IVD and the definition of metrics for ASD's performance evaluation. The IVD's load response with a nonlinear trend is characterized by an initial NZ over which the IVD moves with minimal resistance at small displacements, followed by an EZ with bigger load resistance at bigger displacements. The NZ range is defined as the angle difference between two zero moment points in two loading phases. The slopes of the moment–angle load response in NZ (denoted as red dashed line) and EZ (denoted as green dashed line) are defined as NZ stiffness and EZ stiffness, respectively. Range of motion (ROM) is defined as the maximum displacement or rotational angle from the initial neutral position to the maximally loaded position. The hysteresis area is defined as the area enclosed by the moment–angle curve, while the normalized hysteresis area is calculated by dividing the hysteresis area by the ROM. (For interpretation of the references to color in this figure legend, the reader is referred to the web version of this article.)

Appendix B. Test data analysis

This section explains the test data analysis procedure for deriving the metrics from the measured rotational and compressive load responses of the ASD specimens.

Rotational and compressive test results analysis

In each rotational loading scenario, three cycles of the moment–angle load response of each specimen are recorded, while the first 1.5 cycles are used as pre-conditioning to minimize the effect of viscoelasticity and the specimen's response in the following cycle (1.5–2.5 cycle) is used for data analysis [43]. For the specimens that have rotational response with a significant nonlinear trend, five metrics are derived to describe the specimen's response: NZ range, NZ stiffness, EZ stiffness, normalized hysteresis area, and sigmoidity. While for specimens that have rotational response without distinct NZ and EZ zones, i.e., with a mostly linear load response, NZ stiffness and sigmoidity are left out. The NZ and EZ stiffness are obtained based on a bilinear regression for rotational responses with a nonlinear trend, while the EZ stiffness is obtained based on a linear regression for the load response with a mostly linear trend. For compression responses, the compressive stiffness of each specimen at 4% and 8% strain with each strain rate (0.001, 0.01, 0.02 s^{-1}) is calculated using a linear regression. For each ASD design, the metrics derived from its five specimens are averaged and the corresponding standard deviations are calculated.

Instant helical axis (IHA) and instant center of rotation (ICOR) analysis

Fig. 14 illustrates the movement of the top and end bottom endplates of the specimen from time $t = t_1$ to $t = t_2$ with the fixed global coordinate system ($O_1X_1Y_1Z_1$), the local coordinate system of the bottom endplate ($O_2X_2Y_2Z_2$), and the local coordinate system of the top endplate ($O_3X_3Y_3Z_3$).

In order to describe the rotational response of the specimen, the rotational motion of the top rigid endplate relative to the bottom rigid endplate needs to be calculated. Using homogeneous coordinates, $\mathbf{p}_i = (x_i, y_i, z_i, 1)^{\mathrm{T}}$ denotes a certain point P lying on the top endplate in the coordinate system $O_iX_iY_iZ_i$, and $\mathbf{T}_{ij}$ represents the transformation matrix from coordinate system $O_jX_jY_jZ_j$ to $O_iX_iY_iZ_i$. Thus, the coordinates of point P at time $t = t_1$ and $t = t_2$ can be represented by

$$p_3^{(t_1)} = \left(T_{23}^{(t_1)}\right)^{-1} p_2^{(t_1)}, \tag{1}$$

and

$$p_3^{(t_2)} = \left(T_{23}^{(t_2)}\right)^{-1} p_2^{(t_2)}. \tag{2}$$

Considering that the coordinates of the point P in the coordinate system of the top endplate ($O_3X_3Y_3Z_3$) stay the same from time $t = t_1$ to $t = t_2$, which means $p_3^{(t_1)} = p_3^{(t_2)}$. After substituting Eq. (1) and Eq. (2), it follows:

$$\left(T_{23}^{(t_1)}\right)^{-1} p_2^{(t_1)} = \left(T_{23}^{(t_2)}\right)^{-1} p_2^{(t_2)} \text{ and } p_2^{(t_2)} = T_{23}^{(t_2)} \left(T_{23}^{(t_1)}\right)^{-1} p_2^{(t_1)} \tag{3}$$

Based on Eq. (3), the transformation matrix $\bar{\mathbf{T}}$ from time $t = t_1$ to $t = t_2$ can be expressed as:

$$\bar{T} = T_{23}^{(t_2)} \left(T_{23}^{(t_1)}\right)^{-1}. \tag{4}$$

Considering that

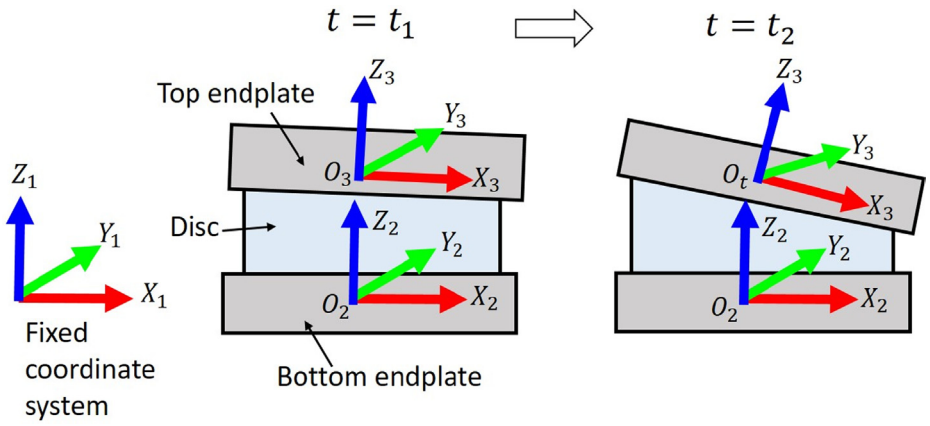

Fig. 14. Coordinate system definition and illustration of the endplates' movement. The three coordinate systems defined are: the fixed global coordinate system ($O_1X_1Y_1Z_1$) and the two local coordinate systems defined on the bottom endplate ($O_2X_2Y_2Z_2$) and on the top endplate ($O_3X_3Y_3Z_3$). The top endplate rotates relative to the bottom endplate from time $t = t_1$ to $t = t_2$, while the bottom endplate is not allowed to rotate.

$$T_{23} = (T_{12})^{-1} T_{13}, \quad (5)$$

the transformation matrix $\bar{\mathbf{T}}$ from time $t = t_1$ to $t = t_2$ is finally expressed as by substituting Eq. (5) into Eq. (4):

$$\bar{T} = (T_{12}^{(t_2)})^{-1} T_{13}^{(t_2)} (T_{13}^{(t_1)})^{-1} T_{12}^{(t_1)}, \quad (6)$$

where$\mathbf{T}_{12}$ and $\mathbf{T}_{13}$ are recorded by the optical tracking system at discrete time points. Afterwards, the IHA is obtained using the method proposed by C. Spoor [64] that calculates the IHA direction based on $\bar{\mathbf{T}}$ at discrete time points calcualted using Eq. (6). To facilitate the comparison of different ASD designs, in each DOF five discrete time points with equal time intervals that span from the neutral positon to the maximally loaded position are used for IHA calculation. Next, the ICOR position is calculated by intersecting the IHAs in flexion/extension, left/right LB, and left/right AR with the sagittal plane, the frontal plane, and the transverse plane, respectively.

Appendix C. Supplementary material

Supplementary data to this article can be found online at https://doi.org/10.1016/j.matdes.2021.110046.

References

[1] Q.-B.B. Bao, G.M. McCullen, P.A. Higham, J.H. Dumbleton, H.A. Yuan, The artificial disc: theory, design and materials., Biomaterials. 17 (1996) 1157–67. https://doi.org/https://doi.org/10.1016/0142-9612(96)84936-2.

[2] A. Faizan, V.K. Goel, S.R. Garfin, C.M. Bono, H. Serhan, A. Biyani, H. Elgafy, M. Krishna, T. Friesem, Do design variations in the artificial disc influence cervical spine biomechanics? A finite element investigation, Eur. Spine J. 21 (S5) (2012) 653–662, https://doi.org/10.1007/s00586-009-1211-6.

[3] M.-A. Rousseau, D.S. Bradford, R. Bertagnoli, S.S. Hu, J.C. Lotz, Disc arthroplasty design influences intervertebral kinematics and facet forces, Spine J. 6 (3) (2006) 258–266, https://doi.org/10.1016/j.spinee.2005.07.004.

[4] A. van Ooij, F.C. Oner, A.J. Verbout, Complications of artificial disc replacement: a report of 27 patients with the SB Charite disc, J. Spinal Disord Tech. 16 (4) (2003) 369–383, https://doi.org/10.1097/00024720-200308000-00009.

[5] G. Denozière, D.N. Ku, Biomechanical comparison between fusion of two vertebrae and implantation of an artificial intervertebral disc, J. Biomech. 39 (4) (2006) 766–775, https://doi.org/10.1016/j.jbiomech.2004.07.039.

[6] Y.A. Othman, R. Verma, S.A. Qureshi, Artificial disc replacement in spine surgery, Ann. Transl. Med. 7 (2019) S170–S170. https://doi.org/10.21037/atm.2019.08.26.

[7] J.-W. Chen, W.-C. Chen, Y.-S. Lai, C.-M. Chang, S.-T. Wang, Effect of a novel compressible artificial disk on biomechanical performance of cervical spine: A finite element study, Adv. Mech. Eng. 7 (2015) 1–5, https://doi.org/10.1177/1687814015602597.

[8] B.W. Cunningham, Basic scientific considerations in total disc arthroplasty, Spine J. 4 (6) (2004) S219–S230, https://doi.org/10.1016/j.spinee.2004.07.015.

[9] M. Skeppholm, L. Lindgren, T. Henriques, L. Vavruch, H. Löfgren, C. Olerud, The Discover artificial disc replacement versus fusion in cervical radiculopathy - A randomized controlled outcome trial with 2-year follow-up, Spine J. 15 (6) (2015) 1284–1294, https://doi.org/10.1016/j.spinee.2015.02.039.

[10] N.A. Langrana, J.R. Parsons, C.K. Lee, M. Vuono-Hawkins, S.W. Yang, H. Alexander, Materials and design concepts for an intervertebral disc spacer. I. fiber-reinforced composite design, J. Appl. Biomater. 5 (2) (1994) 125–132, https://doi.org/10.1002/jab.770050205.

[11] P. O'Leary, M. Nicolakis, M.A. Lorenz, L.I. Voronov, M.R. Zindrick, A. Ghanayem, R.M. Havey, G. Carandang, M. Sartori, I.N. Gaitanis, Response of Charite total disc replacement under physiologic loads: prosthesis component motion patterns, Spine J. 5 (2005) 590–599.

[12] A. Landi, Elastic resistance of the spine: Why does motion preservation surgery almost fail?, World J. Clin. Cases. 1 (2013) 134. https://doi.org/10.12998/wjcc.v1.i4.134.

[13] C.A.M. Jacobs, C.J. Siepe, K. Ito, Viscoelastic cervical total disc replacement devices: Design concepts, Spine J. 20 (12) (2020) 1911–1924, https://doi.org/10.1016/j.spinee.2020.08.007.

[14] J.-Y. Lazennec, A. Aaron, O. Ricart, J.P. Rakover, The innovative viscoelastic CP ESP cervical disk prosthesis with six degrees of freedom: biomechanical concepts, development program and preliminary clinical experience, Eur. J. Orthop. Surg. Traumatol. 26 (1) (2016) 9–19, https://doi.org/10.1007/s00590-015-1695-1.

[15] L. Pimenta, R. Springmuller, C.K. Lee, L. Oliveira, S.E. Roth, W.F. Ogilvie, Clinical performance of an elastomeric lumbar disc replacement: Minimum 12 months follow-up, SAS J. 4 (1) (2010) 16–25, https://doi.org/10.1016/j.esas.2009.12.002.

[16] R.D. Guyer, L.I. Voronov, R.M. Havey, S. Khayatzadeh, G. Carandang, K.R. Blank, S. Werner, J. Rubin, N. Padovani, A.G. Patwardhan, Kinematic assessment of an elastic-core cervical disc prosthesis in one and two-level constructs, JOR Spine. 1 (4) (2018) e1040, https://doi.org/10.1002/jsp2.1040.

[17] P.R. van den Broek, J.M. Huyghe, W. Wilson, K. Ito, Design of next generation total disk replacements, J. Biomech. 45 (1) (2012) 134–140, https://doi.org/10.1016/j.jbiomech.2011.09.017.

[18] P.R. van den Broek, J.M. Huyghe, K. Ito, Biomechanical behavior of a biomimetic artificial intervertebral disc., Spine (Phila. Pa. 1976). 37 (2012) E367-73. https://doi.org/10.1097/BRS.0b013e3182326305.

[19] Z. Yu, K. Shea, T. Stankovic, A computational method for the design of an additively manufactured personalized artificial spinal disc with physiological stiffness under multiple loading conditions, J. Mech. Des. 141 (2019), https://doi.org/10.1115/1.4043931 101406.

[20] M.K. Islam, P.J. Hazell, J.P. Escobedo, H. Wang, Biomimetic armour design strategies for additive manufacturing: a review, Mater. Des. 205 (2021) 109730, https://doi.org/10.1016/j.matdes.2021.109730.

[21] Y. Shikinami, Y. Kotani, B.W. Cunningham, K. Abumi, K. Kaneda, A biomimetic artificial disc with improved mechanical properties compared to biological interverteral discs, Adv. Funct. Mater. 14 (2004) 1039–1046, https://doi.org/10.1002/adfm.200305038.

[22] A. Gloria, R. De Santis, L. Ambrosio, F. Causa, K.E. Tanner, A multi-component fiber-reinforced PHEMA-based hydrogel/HAPEX^{TM} device for customized intervertebral disc prosthesis, J. Biomater. Appl. 25 (8) (2011) 795–810, https://doi.org/10.1177/0885328209360933.

[23] C. Schätz, K. Ritter-Lang, L. Gössel, N. Dreßler, Comparison of single-level and multiple-level outcomes of total disc arthroplasty: 24-month results, Int. J. Spine Surg. 9 (2015). https://doi.org/10.14444/2014.

[24] M.A. Wagner, J.-L. Huang, P. Okle, J. Paik, R. Spolenak, Hinges for origami-inspired structures by multimaterial additive manufacturing, Mater. Des. 191 (2020) 108643, https://doi.org/10.1016/j.matdes.2020.108643.

[25] G. Michaela, H. Denise, M. Liebensteiner, B.C. Michael, Footprint mismatch in lumbar total disc arthroplasty, Eur. Spine J. 17 (11) (2008) 1470–1475, https://doi.org/10.1007/s00586-008-0780-0.

[26] J. Kang, E. Dong, D. Li, S. Dong, C. Zhang, L. Wang, Anisotropy characteristics of microstructures for bone substitutes and porous implants with application of additive manufacturing in orthopaedic, Mater. Des. 191 (2020) 108608, https://doi.org/10.1016/j.matdes.2020.108608.

[27] H. Mehboob, F. Tarlochan, A. Mehboob, S.H. Chang, Finite element modelling and characterization of 3D cellular microstructures for the design of a cementless biomimetic porous hip stem, Mater. Des. 149 (2018) 101–112, https://doi.org/10.1016/j.matdes.2018.04.002.

[28] J. Mueller, K. Shea, Buckling, build orientation, and scaling effects in 3D printed lattices, Mater. Today Commun. 17 (2018) 69–75, https://doi.org/10.1016/j.mtcomm.2018.08.013.

[29] S. Vijayavenkataraman, L.Y. Kuan, W.F. Lu, 3D-printed ceramic triply periodic minimal surface structures for design of functionally graded bone implants, Mater. Des. 191 (2020) 108602, https://doi.org/10.1016/j.matdes.2020.108602.

[30] A. Baldit, Micromechanics of the Intervertebral Disk, Multiscale Biomech. (2018) 455–467, https://doi.org/10.1016/B978-1-78548-208-3.50011-3.

[31] B.K. Bhunia, B.B. Mandal, Modulation of extracellular matrix by annulus fibrosus cells on tailored silk based angle-ply intervertebral disc construct, Mater. Des. 158 (2018) 74–87, https://doi.org/10.1016/j.matdes.2018.08.015.

[32] R. Dittmar, M.M. van Rijsbergen, K. Ito, Moderately degenerated human intervertebral disks exhibit a less geometrically specific collagen fiber orientation distribution, Glob. Spine J. 6 (5) (2016) 439–446, https://doi.org/10.1055/s-0035-1564805.

[33] M.A. Stadelmann, G. Maquer, B. Voumard, A. Grant, D.B. Hackney, P. Vermathen, R.N. Alkalay, P.K. Zysset, Integrating MRI-based geometry, composition and fiber architecture in a finite element model of the human intervertebral disc, J. Mech. Behav. Biomed. Mater. 85 (2018) 37–42, https://doi.org/10.1016/j.jmbbm.2018.05.005.

[34] H.-J. Wilke, K. Wenger, L. Claes, Testing criteria for spinal implants: Recommendations for the standardization of in vitro stability testing of spinal implants, Eur. Spine J. 7 (2) (1998) 148–154, https://doi.org/10.1007/s005860050045.

[35] A.M. Ellingson, D.J. Nuckley, Altered helical axis patterns of the lumbar spine indicate increased instability with disc degeneration, J. Biomech. 48 (2) (2015) 361–369, https://doi.org/10.1016/j.jbiomech.2014.11.010.

[36] W. Anderst, E. Baillargeon, W. Donaldson, J. Lee, J. Kang, Motion path of the instant center of rotation in the cervical spine during in vivo dynamic flexion-extension: Implications for artificial disc design and evaluation of motion quality after arthrodesis, Spine (Phila. Pa. 1976). 38 (2013). https://doi.org/10.1097/BRS.0b013e31828ca5c7.

[37] H. Hwang, J.A. Hipp, P. Ben-Galim, C.A. Reitman, Threshold cervical range-of-motion necessary to detect abnormal intervertebral motion in cervical spine radiographs, Spine (Phila, Pa. 33 (2008) (1976) 261–267, https://doi.org/10.1097/BRS.0b013e31816b88a4.

[38] N. Subramanian, C.A. Reitman, L. Nguyen, J.A. Hipp, Radiographic assessment and quantitative motion analysis of the cervical spine after serial sectioning of the anterior ligamentous structures, Spine (Phila. Pa. 1976). 32 (2007) 518–526. https://doi.org/10.1097/01.brs.0000256449.95667.13.

[39] S.D. Gertzbein, J. Seligman, R. Holtby, K.W. Chan, N. Ogston, A. Kapasouri, M. Tile, Centrode characteristics of the lumbar spine as a function of segmental instability, Clin. Orthop. Relat. Res. 208 (1986) 48–51.

[40] M.-A. Rousseau, D.S. Bradford, T.M. Hadi, K.L. Pedersen, J.C. Lotz, The instant axis of rotation influences facet forces at L5/S1 during flexion/extension and

lateral bending, Eur. Spine J. 15 (3) (2006) 299–307, https://doi.org/10.1007/s00586-005-0935-1.
[41] J. Mueller, K. Shea, C. Daraio, Mechanical properties of parts fabricated with inkjet 3D printing through efficient experimental design, Mater. Des. 86 (2015) 902–912, https://doi.org/10.1016/j.matdes.2015.07.129.
[42] Z. Yu, B. Voumard, K. Shea, T. Stankovic, Dataset of angular and compressive responses of biomimetic artificial spinal discs fabricated using multi-material additive manufacturing, Data Br. (2021).
[43] F. Heuer, H. Schmidt, Z. Klezl, L. Claes, H.-J. Wilke, Stepwise reduction of functional spinal structures increase range of motion and change lordosis angle, J. Biomech. 40 (2) (2007) 271–280, https://doi.org/10.1016/j.jbiomech.2006.01.007.
[44] S.A. Zirbel, D.K. Stolworthy, L.L. Howell, A.E. Bowden, Intervertebral disc degeneration alters lumbar spine segmental stiffness in all modes of loading under a compressive follower load, Spine J. 13 (9) (2013) 1134–1147, https://doi.org/10.1016/j.spinee.2013.02.010.
[45] N. Newell, D. Carpanen, G. Grigoriadis, J.P. Little, S.D. Masouros, Material properties of human lumbar intervertebral discs across strain rates, Spine J. 19 (12) (2019) 2013–2024, https://doi.org/10.1016/j.spinee.2019.07.012.
[46] M.C. Dahl, S. Jacobsen, N. Metcalf, R. Sasso, R.P. Ching, A comparison of the shock-absorbing properties of cervical disc prosthesis bearing materials, ESAS. 5 (2) (2011) 48–54, https://doi.org/10.1016/j.esas.2011.01.002.
[47] O. David, M. Shoham, Compliant Mechanism as a Motion-Preserving Artificial Spinal Disc: A Novel Concept, J. Eng. Sci. Med. Diagnostics Ther. 3 (2020) 1–10, https://doi.org/10.1115/1.4045609.
[48] H. Schmidt, S. Midderhoff, K. Adkins, H.-J. Wilke, The effect of different design concepts in lumbar total disc arthroplasty on the range of motion, facet joint forces and instantaneous center of rotation of a L4–5 segment, Eur. Spine J. 18 (11) (2009) 1695–1705, https://doi.org/10.1007/s00586-009-1146-y.
[49] Y.L. Tee, C. Peng, P. Pille, M. Leary, P. Tran, PolyJet 3D Printing of Composite Materials: Experimental and Modelling Approach, Jom. 72 (3) (2020) 1105–1117, https://doi.org/10.1007/s11837-020-04014-w.
[50] K. Thakare, X. Wei, Z. Pei, Dimensional accuracy in polyjet printing: A literature review, ASME 2019 14th Int. Manuf. Sci. Eng. Conf. MSEC 2019. 1 (2019) 1–7. https://doi.org/10.1115/MSEC2019-3018.
[51] M.R. Silva, A.M. Pereira, Á.M. Sampaio, A.J. Pontes, Assessment of the dimensional and geometric precision of micro-details produced by material jetting, Materials (Basel). 14 (2021) 1–18, https://doi.org/10.3390/ma14081989.
[52] I.A.F. Stokes, M. Gardner-Morse, A database of lumbar spinal mechanical behavior for validation of spinal analytical models, J. Biomech. 49 (5) (2016) 780–785, https://doi.org/10.1016/j.jbiomech.2016.01.035.
[53] G.R. Buttermann, B.P. Beaubien, Biomechanical characterization of an annulus-sparing spinal disc prosthesis, Spine J. 9 (9) (2009) 744–753.
[54] B.P. Beaubien, A. Derincek, W.D. Lew, K.B. Wood, In vitro, biomechanical comparison of an anterior lumbar interbody fusion with an anteriorly placed, low-profile lumbar plate and posteriorly placed pedicle screws or translaminar screws, Spine (Phila. Pa. 1976). 30 (2005) 1846–1851. https://doi.org/10.1097/01.brs.0000174275.95104.12.
[55] A.G. Patwardhan, R.M. Havey, Prosthesis design influences segmental contribution to total cervical motion after cervical disc arthroplasty, Eur. Spine J. 29 (11) (2020) 2713–2721, https://doi.org/10.1007/s00586-019-06064-4.
[56] M.G. Gardner-Morse, I.A. Stokes, Physiological axial compressive preloads increase motion segment stiffness, linearity and hysteresis in all six degrees of freedom for small displacements about the neutral posture, J. Orthop. Res. 21 (3) (2003) 547–552, https://doi.org/10.1016/S0736-0266(02)00199-7.
[57] M. Hsieh, M.R. Begley, L. Valdevit, Architected implant designs for long bones : Advantages of minimal surface-based topologies, Mater. Des. 207 (2021), https://doi.org/10.1016/j.matdes.2021.109838 109838.
[58] H. Schmidt, F. Heuer, H.J. Wilke, Interaction between finite helical axes and facet joint forces under combined loading., Spine (Phila. Pa. 1976). 33 (2008) 2741–2748. https://doi.org/10.1097/brs.0b013e31817c4319.
[59] M. Takahata, Y. Kotani, K. Abumi, Y. Shikinami, T. Kadosawa, K. Kaneda, A. Minami, Bone ingrowth fixation of artificial intervertebral disc consisting of bioceramic-coated three-dimensional fabric, Spine (Phila. Pa. 1976). 28 (2003) 637–644. https://doi.org/10.1097/01.BRS.0000051918.47287.3E.
[60] S.E. Bezci, A. Eleswarapu, E.O. Klineberg, G.D. O'Connell, Contribution of facet joints, axial compression, and composition to human lumbar disc torsion mechanics, J. Orthop. Res. 36 (8) (2018) 2266–2273, https://doi.org/10.1002/jorr.v36.810.1002/jor.23870.
[61] H. Schmidt, F. Galbusera, A. Rohlmann, A. Shirazi-Adl, What have we learned from finite element model studies of lumbar intervertebral discs in the past four decades?, J Biomech. 46 (14) (2013) 2342–2355, https://doi.org/10.1016/j.jbiomech.2013.07.014.
[62] G.A. Holzapfel, C.A.J. Schulze-Bauer, G. Feigl, P. Regitnig, Single lamellar mechanics of the human lumbar anulus fibrosus, Biomech. Model. Mechanobiol. 3 (3) (2005) 125–140, https://doi.org/10.1007/s10237-004-0053-8.
[63] M.M. Panjabi, The stabilizing system of the spine. Part II. neutral zone and instability hypothesis, J. Spinal Disord. 5 (4) (1992) 390–397, https://doi.org/10.1097/00002517-199212000-00002.
[64] C.W. Spoor, F.E. Veldpaus, Rigid body motion calculated from spatial co-ordinates of markers, J. Biomech. 13 (4) (1980) 391–393.